

This is an Open Access document downloaded from ORCA, Cardiff University's institutional repository: <https://orca.cardiff.ac.uk/id/eprint/140146/>

This is the author's version of a work that was submitted to / accepted for publication.

Citation for final published version:

Xie, Zhihua , Lin, Binliang , Falconer, Roger , Nichols, Andrew, Tait, Simon and Horoshenkov, Kirill 2022. Large-eddy simulation of turbulent free surface flow over a gravel bed. *Journal of Hydraulic Research* 60 (2) , pp. 205-219.
10.1080/00221686.2021.1908437

Publishers page: <https://doi.org/10.1080/00221686.2021.1908437>

Please note:

Changes made as a result of publishing processes such as copy-editing, formatting and page numbers may not be reflected in this version. For the definitive version of this publication, please refer to the published source. You are advised to consult the publisher's version if you wish to cite this paper.

This version is being made available in accordance with publisher policies. See <http://orca.cf.ac.uk/policies.html> for usage policies. Copyright and moral rights for publications made available in ORCA are retained by the copyright holders.



To appear in the *Journal of Hydraulic Research*
Vol. 00, No. 00, Month 20XX, 1–23

Research paper

Large-eddy simulation of turbulent free surface flow over a gravel bed

ZHIHUA XIE (IAHR Member), Senior Lecturer, *School of Engineering, Cardiff University, Cardiff, UK*
Email: zxie@cardiff.ac.uk (author for correspondence)

BINLIANG LIN (IAHR Member), Professor, *State Key Laboratory of Hydrosience and Engineering, Department of Hydraulic Engineering, Tsinghua University, Beijing, China; School of Engineering, Cardiff University, Cardiff, UK*
Email: linbl@tsinghua.edu.cn

ROGER A. FALCONER (IAHR Member), Emeritus Professor, *School of Engineering, Cardiff University, Cardiff, UK*
Email: falconerra@cardiff.ac.uk

ANDREW NICHOLS (IAHR Member), Senior Lecturer, *Department of Civil and Structural Engineering, University of Sheffield, Sheffield, UK*
Email: a.nichols@sheffield.ac.uk

SIMON J. TAIT (IAHR Member), Professor, *Department of Civil and Structural Engineering, University of Sheffield, Sheffield, UK*
Email: s.tait@sheffield.ac.uk

KIRILL V. HOROSHENKOV, Professor, *Department of Mechanical Engineering, University of Sheffield, Sheffield, UK*
Email: k.horoshenkov@sheffield.ac.uk

LES of flow over a gravel bed

Large-eddy simulation of turbulent free surface flow over a gravel bed

ABSTRACT

Turbulence in open-channel flow over a gravel bed is highly complex. In this paper, a large-eddy simulation study of turbulent free surface flow over a natural rough bed is presented. A three-dimensional turbulent free surface flow model is employed to study the roughness effects on the turbulence properties and free surface dynamics. The governing equations have been discretised using the finite volume method, with the Cartesian cut-cell method being implemented to deal with the precise scanned gravel bed topography and the deformable free surface being captured by a volume of fluid method. The predicted mean flow velocities and turbulence statistics have been compared with experimental data. A close agreement has been obtained between the two sets of results, providing confirmation that this complementary approach to experimental investigations gives further insight into the turbulent free surface flow dynamics over rough beds. It is found that small waves are generated on the free surface due to the roughness effect for the relative low submergence case.

Keywords: Large-eddy simulation; rough bed; free surface flow; turbulence; open-channel flow; two-phase flow model; Cartesian cut-cell method

1 Introduction

Turbulence occurs in most practical free surface flows. Extensive research has been undertaken to study turbulent flows over rough surfaces (Jimenez, 2004; Powell, 2014) and, in particular, in open-channels (Bathurst, 1985; Ferguson, 2007; Nezu & Nakagawa, 1993; Rodi, Constantinescu, & Stoesser, 2013). However, the current understanding of turbulent open-channel flows over rough beds is still limited, especially in shallow water flows, in which the water depth is similar to, or up to, one order of magnitude higher than the bed roughness. This type of flow is typically found in gravel-bed rivers, with complex surfaces and roughness-turbulent flow-free surface interactions, and is therefore difficult to model and predict. An ability to model accurately the turbulence and free surface dynamics in this type of flow field could enable a better understanding of the transport and mixing of pollutants and sediments.

Many experimental studies of the gravel-bed channel and river flows have been undertaken, particularly over the past two decades, providing useful insights into the mean flow and turbulence statistics for practical engineering applications. Turbulent flows exhibit coherent vortical structures that exist throughout the flow depth (Jimenez, 2018; Stoesser, Braun, Garcia-Villalba, & Rodi, 2008; Tamburrino & Gulliver, 2007). These swirling volumes of fluid are thought to originate from the interaction of the flow with the rough bed boundary (Grass, Stuart, & Mansourtehrani, 1991; Hardy, Best, Lane, & Carbonneau, 2009; Roussinova, Biswas, & Balachandar, 2008). While some researchers have shown that large scale features in the flow are generated by flow separation and form drag in the lee of obstacles, significant bedforms, or dunes (Kostaschuk & Church, 1993; McLean & Nikora, 2006; Muller & Gyr, 1986; Nezu & Nakagawa, 1993), others have shown the existence of large scale turbulent flow structures in the presence of a uniform rough boundary with few or no dominant spatial features, and minimal flow separation (Roy, Biron, Buffin-Belanger, & Levasseur, 1999; Roy, Buffin-Belanger, Lamarre, & Kirkbride, 2004; Shvidchenko & Pender, 2001). These types of flow are dominated by friction drag (grain stress). Hardy et al. (2009) showed that large scale turbulent flow structures were indeed generated over gravel beds and that these structures, initiated at the boundary shear layer, grew and dissipated as they advected and moved upward through the flow depth. These findings are supported by Yalin (1992), who showed the life-cycle of a turbulent structure as it grows from an ejection-induced event at the bottom boundary, into a depth-scale eddy which then breaks down at the free surface into smaller eddies in an energy cascade. Similar behaviour was described by Hardy, Best, Parsons, and Marjoribanks (2016). Some authors argue that the spatial pattern of the time-averaged velocity field is not significantly influenced by the bed boundary roughness at the grain scale and that is instead governed by the relative submergence ratio (Cooper & Tait, 2008; Lamarre & Roy, 2005; Legleiter, Phelps, & Wohl, 2007), while others suggest that the grain scale roughness of the bed is the dominant factor

governing the turbulence properties (Hardy et al., 2009; Hardy, Lane, Ferguson, & Parsons, 2007; Lawless & Robert, 2001a, 2001b; Shah, Agelinchaab, & Tachie, 2008). Recently, different types of surface roughness have also been studied (Li & Li, 2020). Clearly, more research into the nature of turbulent shallow flows over rough beds is required to fully understand the generation mechanisms and effects of coherent structures.

There is a variety of numerical model studies of flow over rough beds as well as some theoretical approaches (Nikora et al., 2007; Papadopoulos, Nikora, Cameron, Stewart, & Gibbins, 2020). Most previous numerical studies have been either based on a two-dimensional (2D) depth-integrated model, in which simple empirical coefficients, such as Chézy, or Manning’s coefficient, have been used to link the mean flow variables to the bed roughness, or the Reynolds-averaged Navier-Stokes equations (RANS), in which roughness effects have been taken into account using the wall function approach and all of the unsteadiness is averaged out and considered as a part of the turbulence through some approximate methods. The biggest limitation in previous models is that the effects of rough elements on turbulent flow and the free surface can not be directly resolved, but have to be parameterized. In addition, the 2D depth-integrated model can not provide full three-dimensional (3D) flow field prediction while the RANS model is difficult to provide instantaneous flow characteristics. In order to overcome these limitations, some direct numerical simulation (DNS) and large-eddy simulation (LES) studies have been undertaken to investigate the flow structure of the turbulence over rough surfaces (Stoesser, 2014). However, most previous studies have been performed for turbulent flows over a well-defined bed roughness, such as square bars (Cui, Patel, & Lin, 2003), a wavy bed (Calhoun & Street, 2001), ripples (Zedler & Street, 2001), one layer of spheres (McSherry, Chua, Stoesser, & Falconer, 2016; Singh, Sandham, & Williams, 2007), sand dunes (Stoesser et al., 2008; Xie, Lin, & Falconer, 2013, 2014; Yue, Lin, & Patel, 2006), sand particles (Schmeeckle, 2014), and the superimposition of different sinusoidal functions (Saccone, Napoli, Milici, & De Marchis, 2019).

Recently, there are also DNS (Thakkar, Busse, & Sandham, 2017) and LES (Alfonsi, Ferraro, Lauria, & Gaudio, 2019; Yuan & Piomelli, 2014) studies reported on scanned rough surfaces. Current DNS simulations are limited to low Reynolds numbers, however, most turbulent flows in gravel beds rivers have Reynolds number of the order 10^5 or higher. In addition, the DNS for a scanned roughness surface (Thakkar et al., 2017) is for an engineered surface which has a small relative roughness and a uniform roughness distribution. These two reasons mean that DNS is still challenging for simulations of real gravel-bed rivers. The LES study on the scanned rough surface (Yuan & Piomelli, 2014) is for a realistic roughness replicated from hydraulic turbine blades, which is different from the nature of real gravel-bed rivers. Recently, Alfonsi et al. (2019) reported a LES study of a pebble bed using the OpenFOAM. For turbulent open-channel flows over a gravel bed, a porosity algorithm has been used by Hardy et al. (2007) and a roughness geometry function together with forcing terms in the momentum equations has been used by Forooghi, Stroh, Magagnato, Jakirlic, and Frohnepfel (2017) for DNS and Stoesser (2010) for LES. However, the porosity and the roughness geometry function methods can not replicate the realistic rough bed, which will affect the flow and turbulence structure in real gravel-bed rivers. In addition, all these DNS and LES gravel bed studies only considered single-phase flow, with a rigid lid approximation for the free surface. The LES study of open-channel flow over a scanned gravel bed with a deformable free surface is rather limited.

The objective of this study is therefore to use the LES approach, combined with a volume of fluid (VOF) method, to investigate the turbulent structure and associated free surface dynamics for open-channel flows over a realistic gravel bed. The natural gravel bed topography in the experimental study by Nichols (2013) is used in the present study, as a series of experiments were undertaken by adjusting the general flow conditions of a range of shallow water flows over a rough sediment boundary, in which the internal flow structures were measured using a combined particle image velocimetry (PIV) and laser induced fluorescence (LIF) approach. A LES model was employed to simulate the same flow conditions as studied experimentally, with the Cartesian cut-cell method

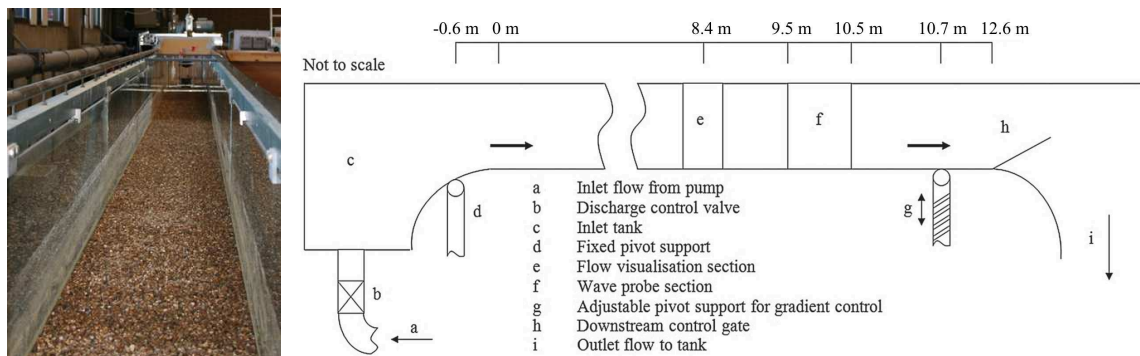


Figure 1: View of the hydraulic flume (left) and schematic of the experimental setup (right).

(Xie & Stoesser, 2020a) being implemented to deal with the actually scanned complex gravel bed topography, which is different from previous studies for well-defined beds or beds generated from a geometric function. In addition, detailed free surface flow dynamics are studied, thanks to the VOF method. Details are given in the remainder of the paper of: (ii) the experimental setup, (iii) the mathematical model and numerical methods, (iv) the computational model setup, (v) the numerical model results, including comparisons with the experimental measurements, mean flow and turbulence statistics, free surface dynamics and the instantaneous vortical structures, effect of relative submergence, and, finally, (vi) some conclusions and future work.

2 Experimental setup

2.1 Laboratory setup

A series of experiments were conducted with a range of shallow flow conditions over a rough, sedimentary boundary being tested. These experiments are concisely summarised here and more details can be found in Nichols (2013) and Nichols, Tait, Horoshenkov, and Shepherd (2016). The experiments were carried out in a 12 m long, sloping rectangular flume (see Fig. 1 for a photograph and the schematic of the experimental setup). The flume was 0.46 m wide and was set to a fixed slope of 0.004. Volumetric flow rates of up to $0.04 \text{ m}^3 \text{ s}^{-1}$ were used in the experiments. The flume had a well-mixed gravel bed placed along the base of the flume, which was composed of washed river gravel with a density of $\rho = 2600 \text{ kg m}^{-3}$ and a median grain size $D_{50} = 4.4 \text{ mm}$. The gravel bed with a uniform thickness was scraped to a uniform level so that its surface had the same slope as the flume. The test section fell in the zone of fully developed flow and the bed surface roughness was measured at the test section of the flume using a laser displacement sensor attached to a computer-controlled scanning frame. During the flow tests, the spatial and temporal patterns of instantaneous streamwise and vertical velocity were measured using PIV.

2.2 Particle image velocimetry

Two-dimensional PIV was used to measure the time-dependent velocity field within the flow, in a vertical plane along the centreline of the flume at 8.4 m from the inlet. This position was 84 to 210 water depths from the flume inlet, where the flow was fully developed. The PIV system was supplied by Dantec Dynamics and used two pulsed 532 nm Nd:YAG (neodymium-doped yttrium aluminium garnet) lasers to illuminate particle motion in a plane within the flow. Plascoat Talisman 30 (a polymer powder normally used for coating metals) was introduced to the flow to act as seeding particles, with a diameter of around $150 \mu\text{m}$ and a narrow particle size distribution. These particles were almost neutrally buoyant, with a specific gravity of 0.99, sufficient to maintain suspension

for several hours in a turbulent flow, and so following the flow path representatively during each measurement.

Two calibrated CCD (charge-coupled device) cameras, each with an image area of 1600 x 600 pixels, were focused on the laser sheet, and were synchronised with the two laser pulses. The cameras were situated a distance of 1.25 m from the light sheet, with an angle of 30° between them. The use of two cameras was to improve on the accuracy of the vertical and streamwise velocity measurements. The overlapping field of view of the two cameras covered an area in the laser plane of approximately 247 mm x 89 mm in the streamwise and vertical directions, respectively. This enabled data to be obtained from an area between 2.5 and 6 water depths long in the streamwise direction for the flow conditions used in this study. This length was generally greater than the typical length of the large scale turbulent structures, given that these were reported to be around 1 to 3 flow depths in length (Cameron, Nikora, & Stewart, 2017; Guala, Hommema, & Adrian, 2006; Kim & Adrian, 1999; Liu, Adrian, & Hanratty, 2001; Nakagawa & Nezu, 1981; Roy et al., 2004). The resolution of the images was approximately 6.5 pixels per mm in either direction. PIV data were collected at a rate of 26.9 Hz for a period of 300 seconds.

Each image pair from the two PIV cameras was divided into interrogation areas of 32 x 32 pixels (with 50% overlap). This interrogation area size corresponded to a physical area of around 4.9 x 4.9 mm, with the overlap meaning the spatial resolution of the measurements was around 2.5 mm in both the streamwise and vertical directions. The mean flow vector for each interrogation area was computed, resulting in a vector field of dimensions 92 x 34 vectors (247 x 89 mm). A two-dimensional cross-correlation technique determined the velocity vector for each interrogation area. The vector maps then underwent range validation with a manually set threshold to remove obviously erroneous data, with fewer than 5% of vectors being removed. A 3 x 3 cell moving average validation was performed with an acceptance factor of 10% to correct any spurious data points and replace the points removed by the range validation (Nichols, 2013).

3 Mathematical model and numerical method

3.1 Governing equations

The LES approach is adopted in this study, and the governing equations used for the incompressible flow are based on the filtered Navier–Stokes equations, given as:

$$\frac{\partial \bar{u}_i}{\partial x_i} = 0, \quad (1)$$

$$\frac{\partial(\rho \bar{u}_i)}{\partial t} + \frac{\partial(\rho \bar{u}_i \bar{u}_j)}{\partial x_j} = -\frac{\partial \bar{p}}{\partial x_i} + \frac{\partial(2\mu \bar{S}_{ij})}{\partial x_j} + \rho g_i + \frac{\partial \tau_{ij}}{\partial x_j}, \quad (2)$$

where the overbar $\bar{\cdot}$ denotes the spatial filtering over the grid, x_i represents the Cartesian coordinates ($i = 1, 2, 3$ corresponding to (x, y, z) , meaning the streamwise, vertical, and spanwise directions, respectively), \bar{u}_i represents the resolved velocity components ($i = 1, 2, 3$ corresponding to \bar{u} , \bar{v} , and \bar{w}), respectively), t is the time, \bar{p} is the filtered pressure, \bar{S}_{ij} is the filtered strain-rate tensor, $g_i = (g \sin(\alpha), -g \cos(\alpha), 0)$ is the gravitational acceleration component in the x_i direction, g is the gravitational acceleration, α is the angle of the channel to the horizontal, ρ and μ are the density and dynamic viscosity of the fluid.

The term $\tau_{ij} = \rho(\bar{u}_i \bar{u}_j - \bar{u}_i \bar{u}_j)$ is the sub-grid scale (SGS) stress tensor and the anisotropic part of the SGS term is modelled by an eddy-viscosity model of the form (Smagorinsky, 1963):

$$\tau_{ij} - \frac{1}{3}\delta_{ij}\tau_{kk} = 2\mu_t\bar{S}_{ij}, \quad (3)$$

where μ_t is the turbulent eddy viscosity defined as:

$$\mu_t = \rho(C_d\bar{\Delta})^2 |\bar{S}|, \text{ and } |\bar{S}| = \sqrt{2\bar{S}_{ij}\bar{S}_{ij}}, \quad (4)$$

with the cut-off length scale $\bar{\Delta} = (\Delta x \Delta y \Delta z)^{1/3}$ and the model coefficient C_d . In this study, the dynamic subgrid model (Germano, Piomelli, Moin, & Cabot, 1991; Lilly, 1992) is used to determine the model coefficient C_d , given as:

$$C_d = \frac{1}{2} \frac{L_{ij}M_{ij}}{M_{ij}M_{ij}}, \quad (5)$$

where $L_{ij} = \widehat{\widehat{u}_i u_j} - \widehat{u_i} \widehat{u_j}$ and $M_{ij} = \widehat{\Delta^2 |\hat{S}| \hat{S}_{ij}} - \bar{\Delta}^2 |\bar{S}| \bar{S}_{ij}$. In these equations, the hat $\widehat{\cdot}$ represents spatial filtering over the test filter. The symbol for spatial filtering $\widehat{\cdot}$ is dropped hereinafter for simplicity.

In order to solve the momentum equation, the fluid property is closed with the constitutive relations for the density and dynamic viscosity of the fluid as given by:

$$\rho = F\rho^w + (1 - F)\rho^a, \quad (6)$$

$$\mu = F\mu^w + (1 - F)\mu^a, \quad (7)$$

where the superscripts ' w ' and ' a ' denote water and air, respectively. F is the volume fraction defined as:

$$F = \begin{cases} 1, & \text{if only fluid water is present;} \\ 0, & \text{if only fluid air is present.} \end{cases} \quad (8)$$

The air-water interface is then within the cells where $0 < F < 1$ and the volume fraction F has a zero material derivative:

$$\frac{dF}{dt} = \frac{\partial F}{\partial t} + u_i \frac{\partial F}{\partial x_i} = 0 \quad (9)$$

These equations complete the mathematical description of the turbulent free surface flow model used in the present study.

3.2 Numerical method

For the sake of brevity, only a brief description of the numerical method is presented here, and more details of the in-house 3D two-phase flow code (Xdolphin3D) can be found in previous works (Xie, 2012, 2015; Xie & Stoesser, 2020a; Xie, Stoesser, Yan, Ma, & Lin, 2020). In the present study, the filtered Navier-Stokes equations (Eq. 1 and Eq. 2) were discretised using the finite volume method on a staggered Cartesian grid. The advection terms were discretised using a high-resolution scheme (Xie, 2012), combining high order accuracy with monotonicity (a hybrid first-order upwind and a high-order scheme with a flux limiter), whereas the gradients in the pressure and diffusion terms were obtained using a central difference scheme. The SIMPLE algorithm (Patankar, 1980) was employed for the pressure-velocity coupling, with the second-order backward difference method being used for the time derivative, thus leading to an implicit scheme for the governing equations. In this study, the air-water interface (Eq. 9) is captured by a high-resolution volume of fluid (VOF) scheme CICSAM (Compressive Interface Capturing Scheme for Arbitrary Meshes) (Ubbink, 1997), which does not need to reconstruct the interface after each time step. This scheme can take into account the deformation of the free surface in open-channel flows. The VOF scheme can also be switched off in the present model when considering the rigid lid approximation by using the free-slip boundary condition at the free surface. The code was parallelised using MPI (Message Passing Interface) and a domain decomposition technique.

To deal with complex topography in engineering applications, overlapping grids, boundary-fitted grids, and unstructured grids can be used. These methods provide great flexibility to conform onto complex stationary or moving boundaries. However, the programming of these methods can be complicated and generating such a grid is usually very cumbersome (Mittal & Iaccarino, 2005). Cartesian grid methods, which can simulate flow with a complex topography on Cartesian grids, avoid these problems. Two of the most popular methods are the immersed boundary method (Mittal & Iaccarino, 2005) and the Cartesian cut cell method (Ingram, Causon, & Mingham, 2003). The primary advantage of a Cartesian grid method is that only moderate modification of the program on Cartesian grids is needed to account for a complex topography. A Cartesian grid method also has the advantage of being simple to generate, particularly with moving boundary problems, due to the use of stationary, non-deforming grids. However, the drawback of this method is that implementing boundary conditions is not straightforward. For LES studies of turbulent flow over rough surfaces, boundary-fitted grids (Stoesser et al., 2008; Yue, Lin, & Patel, 2005a, 2005b; Yue et al., 2006) and the immersed boundary method (Nikora et al., 2019) have been previously used. In the present study, the Cartesian cut-cell method (Xie & Stoesser, 2020a) has been utilised with a θ function being introduced in the finite volume discretisation for a structured grid. The θ function is defined in such a manner that the value is 1 for a point accessible to the fluid and 0 for a point under the gravel bed surface. The average of θ over a control volume, or cell face, is the fraction of the volume, or area, available to the flow. In cut-cells such as the interface for the gravel bed, the advective and diffusive fluxes at cell faces, as well as their cell volumes, have to be modified and more details are given for fixed (Xie, 2015) and moving (Xie & Stoesser, 2020a) geometries.

The code Xdolphin3D was validated and applied for some LES studies of open-channel flows over well-defined regular roughness (Xie, Lin, & Falconer, 2013; Xie et al., 2014; Xie, Lin, Falconer, & Maddux, 2013). In addition, the present model has been validated against available experimental data for a range of free surface flow problems, such as overturning waves over a sloping beach and a reef (Xie, 2012), periodic breaking waves in the surf zone (Xie, 2013), breaking solitary waves over 3D conical structures (Xie & Stoesser, 2020b) and complex topography (Xie, 2015), in which the overturning jet, air entrainment and splash-up have been captured during wave breaking. Recently, Xdolphin3D has been applied for two-phase flow with moving bodies (Xie & Stoesser, 2020a) and LES of wave-structure interaction problems (Xie et al., 2020).

4 Computational setup

The computational model was set up to replicate the flows in the laboratory model studies described in [Section 2](#). As the focus on the present study was to investigate the roughness effect on free surface flows, the lowest flow submergence case was considered herein. The maximum water depth h (relative to the mean bed elevation) was 0.039 m, with the ratio of the water depth h to the maximum gravel height H , i.e. h/H , being 2.8. In the simulation, the physical properties of the water and air were taken as: $\rho^w = 998 \text{ kg m}^{-3}$ and $\mu^w = 8.89 \times 10^{-4} \text{ kg m}^{-1}\text{s}^{-1}$ for water; and $\rho^a = 1.185 \text{ kg m}^{-3}$ and $\mu^a = 1.83 \times 10^{-5} \text{ kg m}^{-1}\text{s}^{-1}$ for air. The corresponding Reynolds and Froude numbers, based on the mean bulk flow velocity $U_{bulk} = 0.33 \text{ m s}^{-1}$ and the maximum water depth h , were $\text{Re} = 14,448$ and $\text{Fr} = 0.53$, respectively.

The photograph of the test section in the flume and detailed scanned profile of the gravel bed are shown in [Fig. 2a](#) and [Fig. 2b](#), respectively. It is worth noting that the present study aims to resolve the superstructure formed by the grains rather than that for each single grain, so the rough impermeable bed is considered as a whole. An example of the schematic view of the computational domain is shown in [Fig. 2c](#), where the origin is located at the mean gravel bed elevation, at the upstream section along the central plane. A section of the gravel bed of length $L_x = 0.4 \text{ m}$ (covering 10 times the water depth) and width $L_z = 0.2 \text{ m}$ was selected from the test section in the experiments (dashed line area in [Fig. 2b](#)) in order to avoid wall effects (shown in [Fig. 2c](#)). The height of the computational domain $L_y = 0.07 \text{ m}$ is considered here, which covers all of the regions for the gravel bed, water, and air. It can be seen that the scanned rough bed is successfully inputted as an immersed boundary in the computational model using the Cartesian cut-cell method ([Xie & Stoesser, 2020a](#)) and an example of the cut cell to deal with the bed elevation along the central plane is shown in [Fig. 2d](#), where both the area and volume available to the flow at each cell are calculated.

The computational domain of $L_x \times L_y \times L_z$ ($0.4 \times 0.07 \times 0.2 \text{ m}^3$) for this submergence case was discretised using a uniform structured grid of $256 \times 96 \times 128$ points in the streamwise, vertical, and spanwise directions, respectively. In the simulation, same mesh sizes were used in the horizontal plane and they were approximately 2.1 times the mesh size in the vertical direction ($\Delta x = \Delta z \approx 2.1\Delta y$). Approximately 24 cells were selected to cover the height of the rough bed in the vertical direction, which has been shown to capture most of the turbulent structures in the rough boundary ([Xie et al., 2014](#); [Xie, Lin, Falconer, & Maddux, 2013](#)). A time step with Courant-Friedrichs-Lewy (CFL) number of 0.1 was used in the simulation in order to accurately capture the free-surface dynamics. Periodic boundary conditions were used in the streamwise and spanwise directions in order to reduce the computational effort. It is worth noting that the periodic, rather than the wall boundary condition was used in the spanwise direction due to the width of the computational domain (0.2 m) being less than the width of the actual flume (0.46 m). As both fluids in the air and water, were solved simultaneously in the present two-phase flow model, the kinematic and dynamic free surface boundary conditions were already implemented, with the air-water interface being captured by the VOF method. They differed from the rigid lid treatment being used in previous LES studies of turbulent open-channel flows (e.g. [Hardy et al., 2007](#); [Nikora et al., 2019](#); [Stoesser, 2010](#); [Zedler & Street, 2001](#)). The simulations were performed using 256 cores in the Supercomputing Wales cluster at Cardiff University and the computing time was approximately 72 hours.

5 Results and discussion

In this section, both numerical and experimental results are presented of the turbulent free surface flow structure, predicted and measured over the gravel bed. The instantaneous results are shown first and then the time-averaged and space-time-averaged (double-averaging) ([Nikora et al., 2007](#))

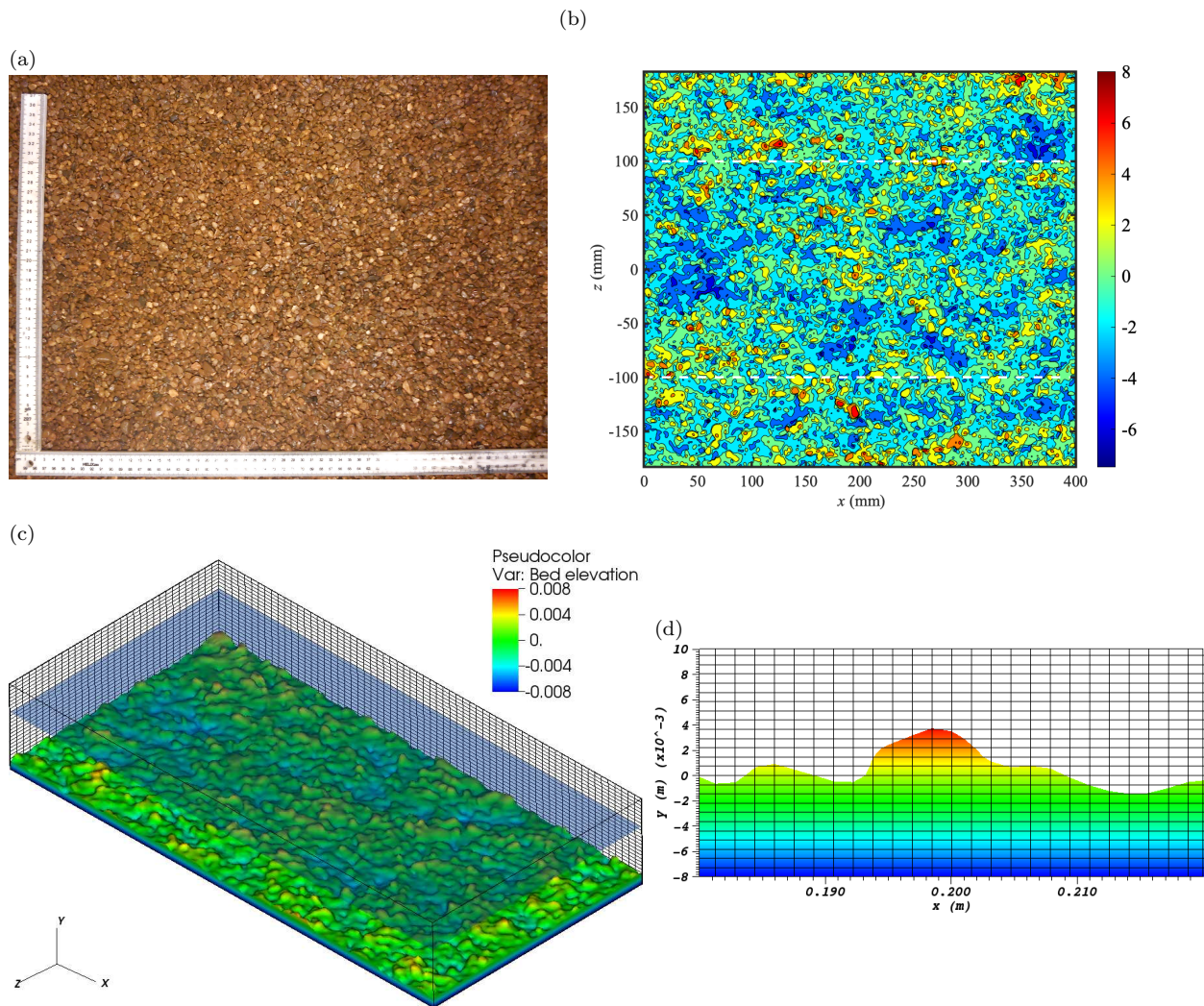


Figure 2: A photograph of the test section in the hydraulic flume (a); gravel bed profile in the test section measured by the digital elevation method, in which the region bounded by the dashed line is inputted to numerical model (b); the schematic view of the computational domain for the low submergence case with the numerically-generated gravel bed elevation given in metres (only every fourth grid lines are plotted) (c); and an example of the cut-cell method to deal with the bed topography in the middle of the central plane (d).

results are presented later. Finally, the vortical structures and the effect of relative submergence are discussed. In the following, the overbar, i.e.: $\bar{\cdot}$, represents averaging over time, and the resolved variable ϕ is decomposed into a mean value and a resolved fluctuation as: $\phi = \bar{\phi} + \phi'$, where the prime denotes fluctuation with respect to the mean resolved quantity. A subscript letter $i = x, y, z$, followed by angular brackets ($\langle \cdot \rangle$), implies additional spatial averaging of the mean value $\bar{\phi}$ over the streamwise ($\langle \bar{\phi} \rangle_x$), vertical ($\langle \bar{\phi} \rangle_y$), and spanwise ($\langle \bar{\phi} \rangle_z$) directions, respectively. It is worth noting that streamwise and spanwise averaging is performed at fixed depth levels, with only the flow variables located above the gravel bed being taken into account.

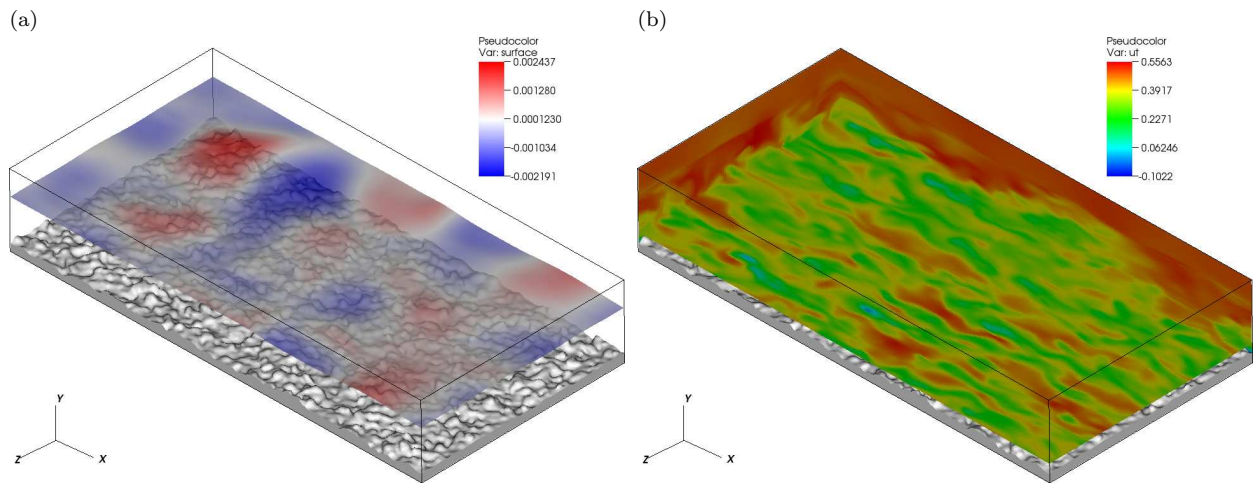


Figure 3: Instantaneous water surface profile for the flow over the gravel bed (a); and contours of the instantaneous streamwise velocity u (m/s) along three slices ($x = 0$ m, $y = 0.01$ m, and $z = 0$ m) for the low submergence case $h/H = 2.8$.

5.1 Instantaneous flow fields

As the topography of the gravel bed is complex, the flow above the bed in the flume is chaotic and highly turbulent. Fig. 3a shows an example of an instantaneous snapshot for the water surface profile above the gravel bed captured by the VOF method. It can be seen that small waves are generated for the flow above the rough surface, which is different from the normally used rigid-lid approximation for most open-channel flow simulations. The wavy interface has three-dimensional features with streamwise and spanwise variations. The instantaneous wave height is approximately 11% of the water depth, which demonstrates the effect of the low submergence of the flow. The amplitude of the waves is similar to a similar low submergence of flow over a 2D dune (Xie et al., 2014), although they have a different type of rough beds. Fig. 3b shows an instantaneous snapshot for the model predicted instantaneous streamwise velocity for the flow. The contours of the value for three slices in different directions (i.e. two vertical planes at $x = 0$ m and $z = 0$ m and one horizontal plane just above the peak of the gravel surface at $y = 0.01$ m) are shown together with the bed topography profile. It can be seen that the streamwise velocity is small close to the gravel bed and gradually increases in the vertical direction, which is expected behaviour. The streamwise velocity changes direction in some local regions just above the peak gravel bed, which is due to the flow separation being generated downstream of the peak of the local bed. It can also be observed from the horizontal plane that an alternating pattern for the streamwise velocity is generated in the spanwise direction, indicating that streaks are formed in the near-wall region and are similar to the actual velocity structural patterns measured by Cooper and Tait (2008), which is the dominant mechanism for the production of the turbulent structure in open-channel flows. These long streaky structures near the bed have similar spacing as those observed for wall turbulence in channels and pipes (Guala et al., 2006), and gradually increase along with the water depth.

5.2 Time-averaged flow fields

In order to investigate the mean velocity profile above the gravel bed, the time-averaged streamwise velocities \bar{u} along the central plane are shown in Fig. 4a and Fig. 4b, in which the PIV experimental results are shown in Fig. 4a, while the LES predicted results are shown in Fig. 4b. The local bed topography is also included at the bottom of each plot. It is worth noting that experimental measurements were not available in the vicinity of the bed and near the free surface due to the

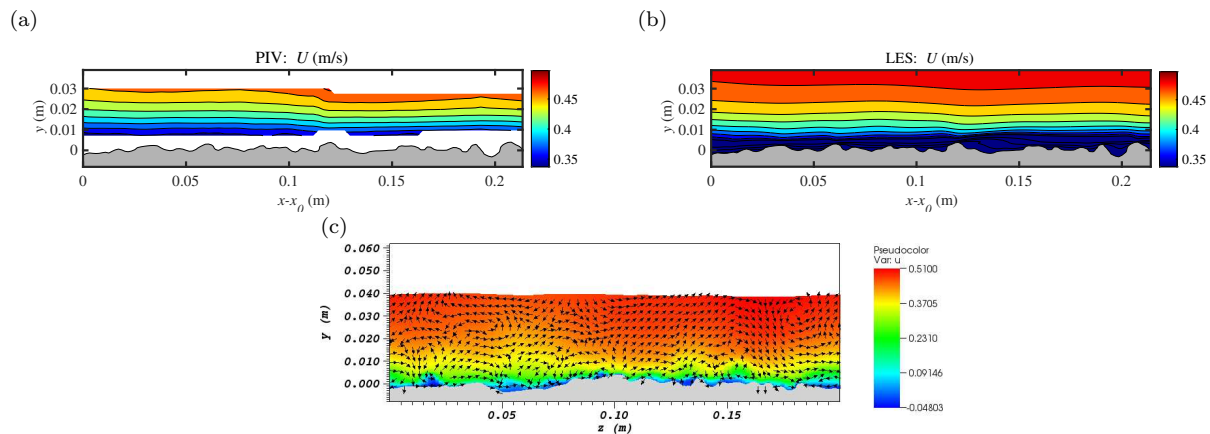


Figure 4: Comparison for the time-averaged streamwise velocity \bar{u} along the central plane between the PIV (a) and LES (b) results for the low submergence cases. x_0 is the starting point of the test section; and (c) the time-averaged streamwise velocity \bar{u} along the cross section ($x = 0.2$ m) together with the secondary current (\bar{v}, \bar{w}) .

experimental limitations. This limitation is not included in the numerical model, which provides results for the whole domain to better understand the hydrodynamics of this type of flow.

It can be seen from Fig. 4 that the mean streamwise velocity is more uniformly distributed above the gravel bed, which is markedly different from the instantaneous streamwise velocity shown along the central plane in Fig. 3b. The velocity is small in the near-bed region and gradually increases with an increase in the water depth. At a certain water depth, the mean velocity is not uniform in the streamwise direction, corresponding to the bed topography below. It can be seen that there is a significant effect of the rough bed on the mean velocity profile, which is different from the usually presented open-channel flow over a smooth bed. A good agreement is obtained between the experimental measurements and numerical predictions for this case, even for the trend of increasing or decreasing the mean velocity at some locations along the gravel bed.

Figure 4c presents the contour of the time-averaged streamwise velocity \bar{u} with velocity vectors (\bar{v}, \bar{w}) along the vertical cross section. It can be seen that the streamwise velocity distribution in the cross section is similar to that along the central plane, with its minimum value near the gravel bed. Some parts of the region have a negative mean streamwise velocity, which means that there is flow separation due to the bed topography. Secondary currents are observed in the LES simulations and large magnitude of vectors are predicted close to the gravel bed (it is worth noting that for the sake of clarity, only the flow pattern is shown here and the velocity vectors are not normalised by their magnitudes). As the experimental measurements were only along the central plane, the LES results could act as a complementary approach to study detailed flow phenomena in other regions, especially in the vicinity of the rough bed and the free surface.

5.3 Double-averaged flow fields and turbulence statistics

Because the flow is spatially heterogeneous, but with uniform flow depth, the double-averaging (in both time and space) methodology (Nikora et al., 2007) is employed in this section to analyse the results, where the approach has been based on the spatial averaging of the time-averaged value over the whole computational domain (which is $\langle \bar{\phi} \rangle_{xz}$), and which is expected to provide a representative value for the flow. In addition to the VOF simulation, a rigid lid simulation was also carried out in order to compare the free surface effect. Fig. 5 shows the predicted vertical profiles of the double-averaged streamwise velocity ($\langle \bar{u} \rangle$), turbulence strength ($\langle \sqrt{u'^2} \rangle$ and $\langle \sqrt{v'^2} \rangle$) and Reynolds shear stress ($\langle -u'v' \rangle$), along with corresponding experimental measurements.

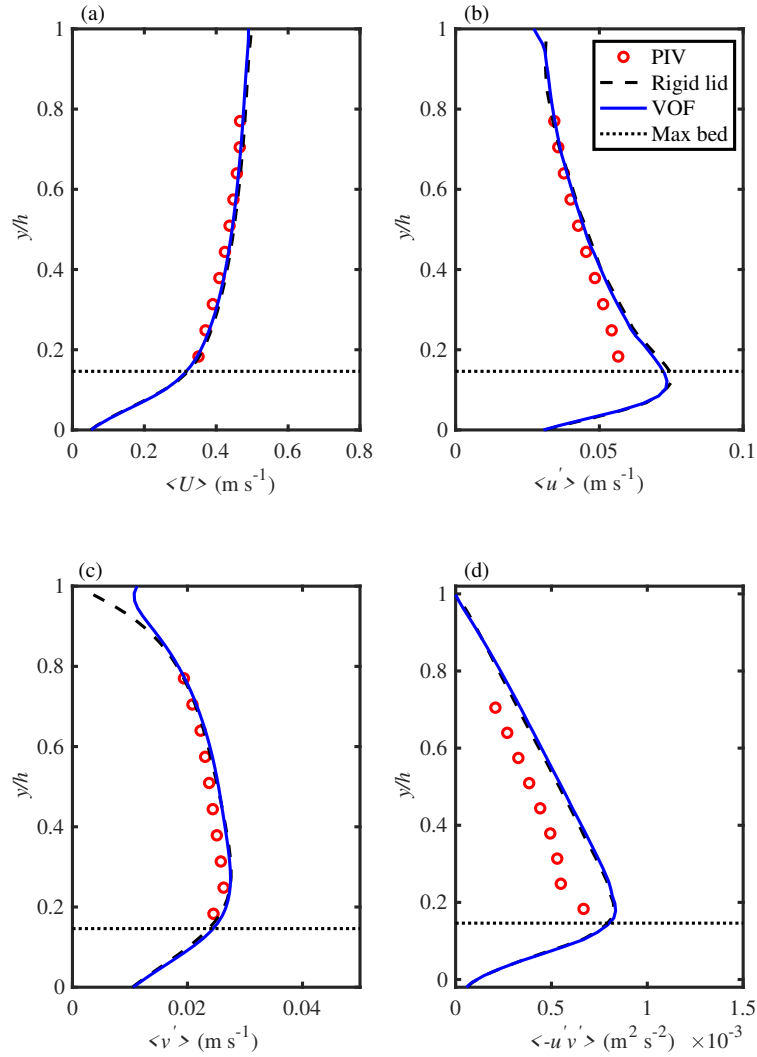


Figure 5: Comparison of the double-averaged streamwise velocity (a), streamwise turbulence intensity (b), vertical turbulence intensity (c) and Reynolds stress (d) between experimental measurements and numerical model results for the VOF and the rigid lid simulations.

It is shown in Fig. 5 that the mean velocity $\langle \bar{u} \rangle$ exhibits a linear profile below the maximum gravel bed elevation (denoted as dotted lines) in the near-bed region and a logarithmic profile in the outer layer (this can also be seen later when plotted as semi-logarithmic type in Fig. 8). The mean velocity is accurately predicted above the maximum gravel bed elevation for both simulations. The streamwise turbulence intensity attains its peak value just below the maximum bed elevation and decreases towards both the free surface and the bed. The $\langle \sqrt{u'^2} \rangle$ is slightly over-predicted using the present model near the maximum bed elevation but a better result is obtained from the VOF simulation. The vertical turbulence intensity increases from the bottom to a height above the maximum bed elevation, which then decreases towards the free surface. The modelled $\langle \sqrt{v'^2} \rangle$ is well predicted in the lower region of the flow for both simulations and towards the free surface. By comparing the two simulation results, it is worth noting that at the free surface there is a significant

difference between the vertical turbulence intensities predicted by the rigid lid and deformable free surface approaches, mainly based on physical reasoning. In a rigid lid approximation, $\langle \sqrt{v'^2} \rangle$ approaches zero at the free surface according to the free-slip boundary condition. However, $\langle \sqrt{v'^2} \rangle$ is not zero at the free surface in the VOF simulations, as the air-water interface is deformable, which is more physically reasonable. The peak value of the Reynolds shear stress is found to occur at a short distance above the maximum bed elevation and similar trends are observed between the predicted and measured results. However, the Reynolds stress component $\langle -u'v' \rangle$ is over-predicted by the present model. This discrepancy might be attributed to the fact that the periodic boundary conditions used in the simulations were different from the actual flow conditions in the experiment, and which could have enhanced the turbulence levels in the simulations. Another reason might be that the PIV measurement is along a section of the central plane whereas the whole 3D computational domain is used for the spatial averaging.

Overall, a good agreement between the experimental measurements and the predicted results for the double-averaged streamwise velocity $\langle \bar{u} \rangle$ is obtained in this study, whereas reasonable agreement is obtained for the turbulence statistics. As the velocity within the roughness layer is very difficult to measure, the LES model can be used as an additional tool to study the details for the near-bed flow.

5.4 Vortical structures

The large-scale coherent structures generated over the gravel bed play an essential role in the interaction between the bed and free surface, sediment transport, and bedform evolution in open-channel flows. These coherent structures are mainly responsible for maintenance of turbulence (through production and dissipation) in the turbulent boundary layer (Robinson, 1991). It is suggested that hairpin vortices originate from the near-wall region concatenate to form packets and then large-scale motions (LSMs), which eventually concatenate to form very large-scale motions (VLSMs), ranging between 2 and 1214 pipe radius (Guala et al., 2006; Kim & Adrian, 1999). Recently, Cameron et al. (2017) investigated the LSMs and VLSMs in rough-bed open-channel flows and found that LSMs scale with the flow depth whereas VLSMs might depend on additional scales (e.g. channel width, roughness height, or viscous length). Ferraro, Coscarella, and Gaudio (2019) also studied the turbulence scales for open-channel flows with low submergence and they found a peak for VLSMs but without any bimodal distribution. In order to illustrate the coherent vortical structure developed in the flow over the gravel bed, the λ_2 method (Jeong & Hussain, 1995) was used in the present study to identify vortex cores, based on the second invariant of the velocity gradient tensor. Fig. 6 shows an example of snapshots of the water surface and vortical structures in the water column, in which the vortical structures are coloured by the vertical distance y and the water surface is coloured by the vertical distance to the mean water depth h . It can be seen that hairpins and elongated quasi-streamwise vortical structure are generated in the near-bed region, which are the main contribution for the Reynolds shear stresses. They are advected downstream, with complex temporal and spatial interactions occurring between these vortical structures, and concatenate to form vortex packets for LSMs (Kim & Adrian, 1999). Some of these vortical structures move with an upward tilt and eventually interact with the deformable free surface (shown as red structures on the free surface). The temporal and spatial evolution of the free surface can also be seen in Fig. 6, with surface waves being observed during the simulations. Surface renewal, such as upwelling and downdraft, can be seen on the water surface (Nichols, 2013). It is worth noting that the VOF simulations provide a useful tool to study the free-surface dynamics, which is often neglected in most open-channel flow simulations.

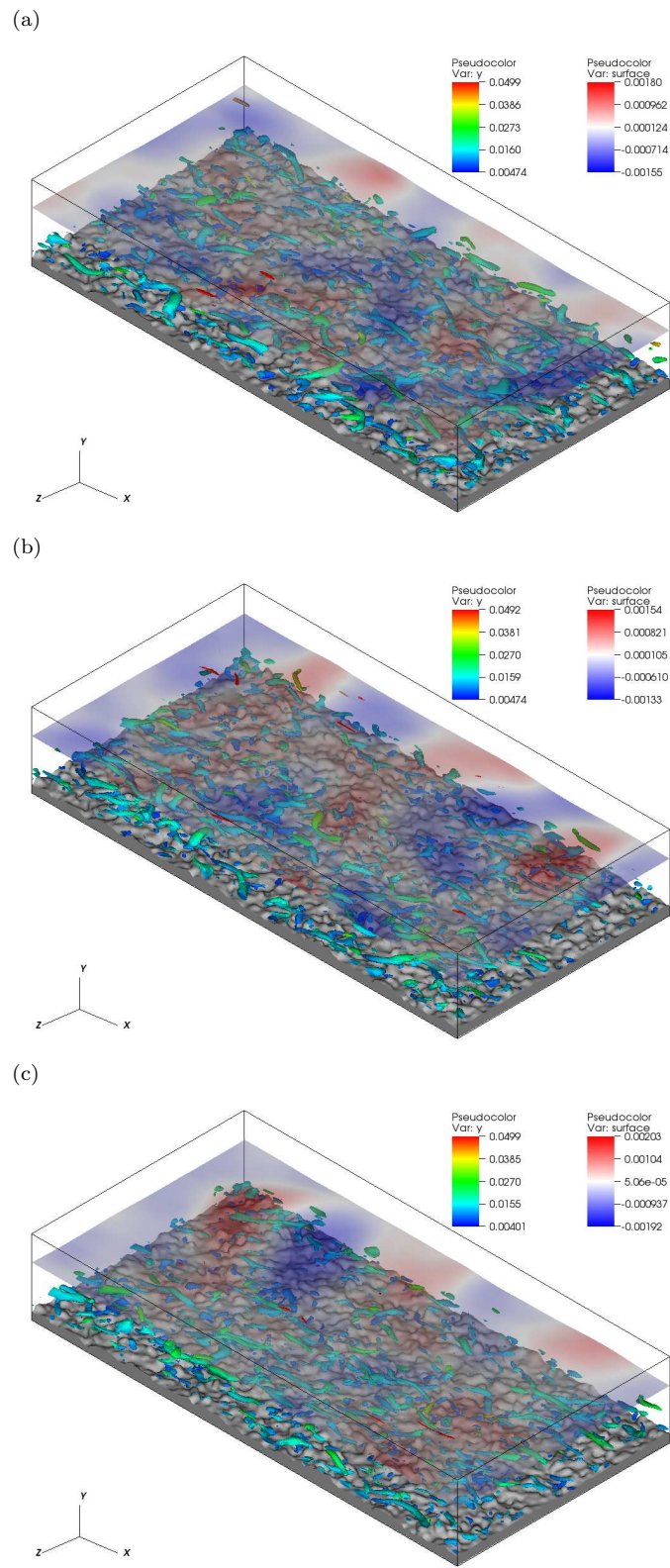


Figure 6: Snapshots of water surface and vortical structures in water column. The time interval between snapshots is 0.2 s.

5.5 Effect of relative submergence on the mean and turbulence statistics

In order to study the effect of relative submergence on turbulent open-channel flows, three submergence ratio cases (shown in Table 1), denoted as low, mid and high, were selected for cross comparison, with the ratio of the water depth h (relative to the mean bed elevation) to the maximum gravel height H , i.e. h/H , being 2.8, 5.1 and 7.3, respectively. It is worth noting that only rigid lid simulations are presented here due to computational efforts, as the focus here is the effect of relative submergence and the free surface effect would become less significant when increasing the water depth.

Table 1: A summary of the experimental conditions for the flow over a gravel bed with $D_{50} = 4.4$ mm. $\delta\nu$ is the thickness of the laminar sublayer and k_s is the equivalent roughness.

Case	Slope S	Depth h (m)	h/H	U_{bulk} (m s ⁻¹)	$\delta\nu$ (mm)	k_s (mm)	Re	Fr
low	0.004	0.039	2.8	0.33	0.265	4.9	14,448	0.53
mid	0.004	0.070	5.1	0.50	0.197	3.7	39,291	0.60
high	0.004	0.100	7.3	0.65	0.165	3.0	72,970	0.65

Figure 7 shows the predicted vertical profiles of the double-averaged streamwise velocity ($\langle\bar{u}\rangle$), turbulence strength ($\langle\sqrt{u'^2}\rangle$ and $\langle\sqrt{v'^2}\rangle$) and Reynolds shear stress ($\langle-\overline{u'v'}\rangle$), along with the corresponding experimental measurements. Three different relative submergence cases are shown in Fig. 7, where the horizontal axis is normalised through the mean depth-averaged velocity U_m for each case and the vertical axis is normalised using the water depth h , respectively.

It is shown in Fig. 7 that the mean velocity and turbulence statistics follow the similar trend shown for the VOF simulation for the low submergence case in Fig. 5. It is also worth noting that the double-averaged velocities $\langle\bar{u}\rangle$ are almost identical above the maximum gravel bed elevation and there is only a slight difference between the results in the roughness layer due to the spatial variation of the gravel bed. The mean velocity has a relatively larger magnitude in the roughness layer for the high submergence case. For the turbulence statistics, all three cases have similar distribution above the maximum gravel bed elevation and the main difference is in the roughness layer, which is due to the relative submergence of the rough bed. Overall, reasonably good agreement is obtained between the LES and PIV results for the turbulence statistics.

In order to compare the velocity distribution between rough- and smooth-bed flows, Fig. 8 presents the vertical distribution of the double-averaged velocity $\langle\bar{u}\rangle$ in a linear-linear and semi-logarithmic type plots, where the horizontal axis is normalised by the bed roughness H and the mean velocity is normalised by the friction velocity u^* ($u^* = \sqrt{gSh}$ is used here) although there are some other velocity scales (Ferraro, Servidio, & Gaudio, 2019). The smooth-wall linear and logarithmic laws are also plotted in Fig. 8 for reference (when $C = 11.1$). It can be seen from Fig. 8a that in the roughness layer, the double-averaged streamwise velocity follows the linear distribution, similar to the smooth-bed flows but with a different slope. Above the roughness layer, the velocity follows the smooth-bed logarithmic law but with different roughness effect (i.e. different C values). This is consistent with the theoretical derivation of the velocity distribution for 2D, steady, uniform, spatially averaged flow over a rough bed with a flat free surface (Nikora, Goring, McEwan, & Griffiths, 2001). It can be seen from Fig. 8 that the normalised streamwise velocity decreases with the increase in the relative submergence ratio and this is mainly related to higher Re numbers for the high submergence flow. The value C will decrease for rough-bed flow when compared to smooth-bed flows and with the smallest value being obtained for the highest Re number flow case. It is also observed from Fig. 8b that the relative submergence has an effect on the von Kármán constant κ value (0.41 for smooth-bed flows) as the slope for the logarithmic plot is slightly different, especially for the low submergence case, which is consistent with the experimental

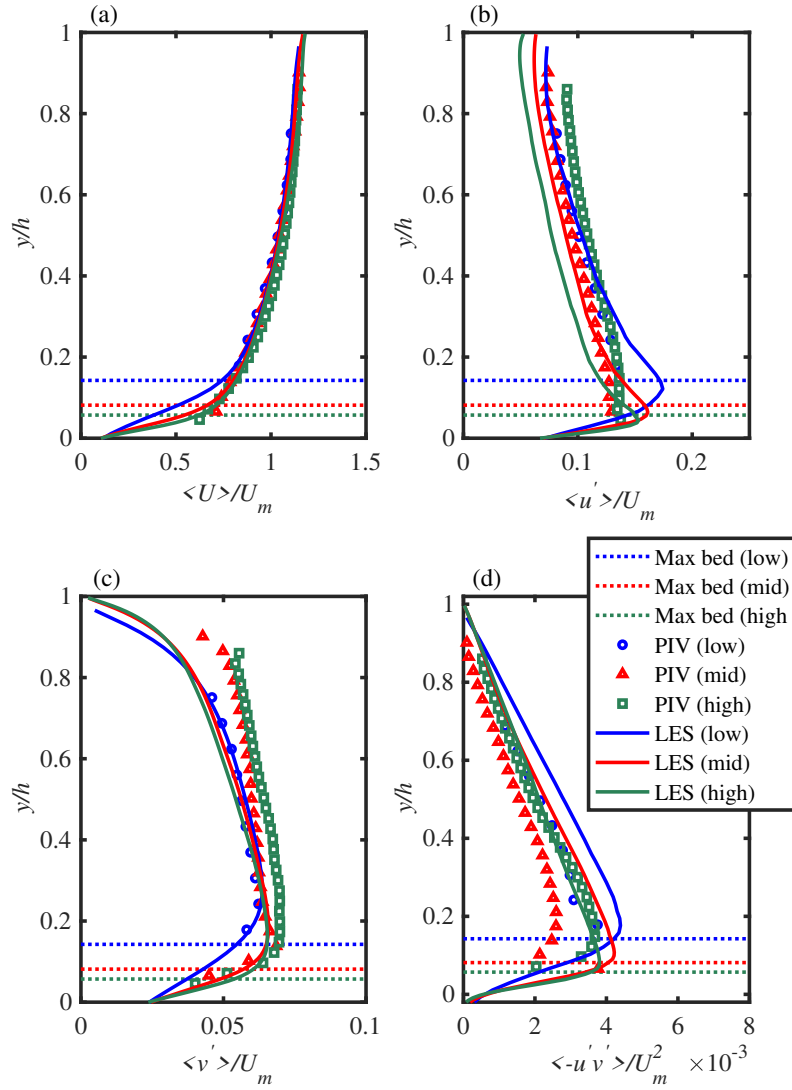


Figure 7: Comparison of the double-averaged streamwise velocity (a), streamwise turbulence intensity (b), vertical turbulence intensity (c) and Reynolds stress (d) between experimental measurements and numerical model results for the low (blue colour), mid (red colour), and high (green colour) submergence cases.

findings for low submergence rough-bed open-channel flows (Cameron et al., 2017).

As the friction factor f is very important in rough-bed open channel flows, Fig. 9 shows a comparison of the friction factor estimates using PIV and LES data. It can be seen that good agreement between the PIV and LES data are obtained (within 5% error range). As expected, the friction factor decreases with the increase in the water depth, showing that the roughness effect is less important in high submergence flows.

Figure 10 shows the correlation coefficient $\left(\frac{\langle -u'v' \rangle}{\langle \sqrt{u'^2} \rangle \langle \sqrt{v'^2} \rangle}\right)$ for the three submergence cases. Nezu and Nakagawa (1993) mentioned that for most flow and roughness types, the correlation coefficient should increase gradually with the depth of water (y/h), decrease in the vicinity of the free surface

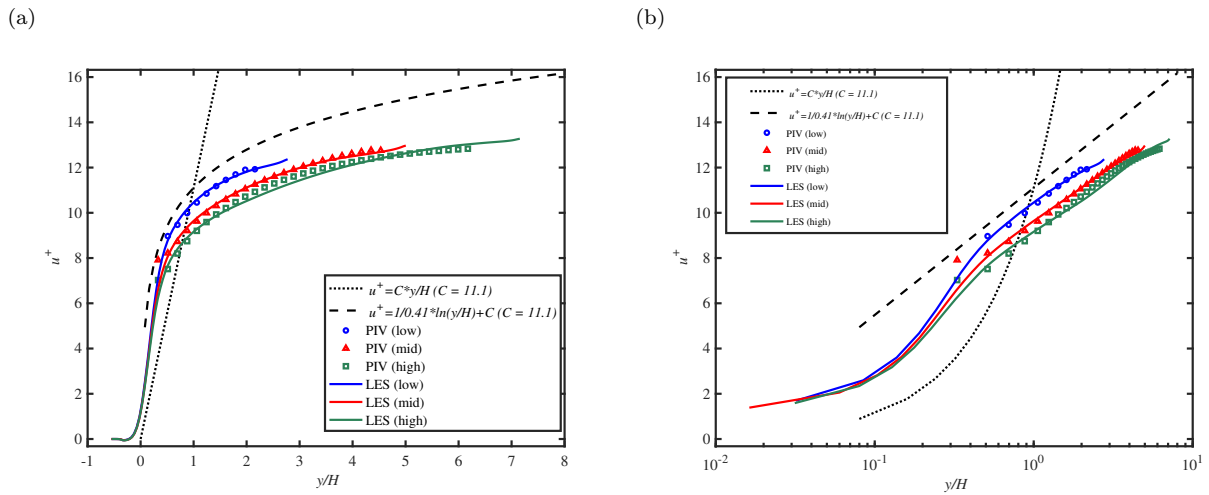


Figure 8: Comparison of double-averaged streamwise velocities between experimental measurements and numerical model results in linear-linear (a) and semi-logarithmic (b) plots. The dotted and dashed lines are for law of the wall for smooth surfaces.

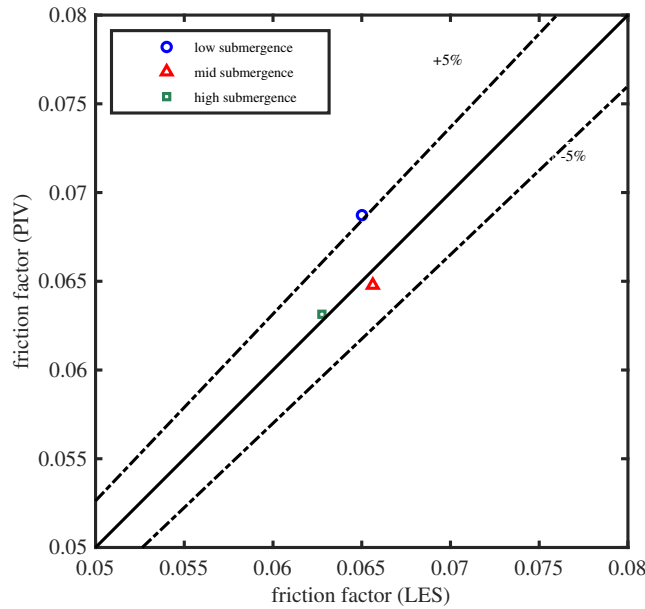


Figure 9: Comparison of the friction factor estimates using PIV and LES data for the low (blue color), mid (red color), and high (green color) submergence cases.

region, and be kept nearly constant (around 0.4) in the intermediate region. It can be seen that the obtained results agree well with Nezu and Nakagawa (1993) and the experimental measurements (Nezu, 1977) over the whole water depth. There is a critical point $y/h \approx 0.2$, at which the relative submergence ratio has a different effect on the correlation coefficient.

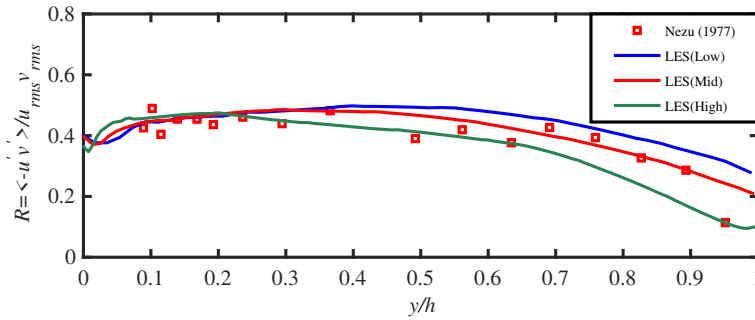


Figure 10: Comparison of the predicted correlation compared with experimental measurements (Nezu, 1977).

6 Conclusion

In this study large-eddy simulations of turbulent free surface flow over a natural rough bed have been presented, with a good agreement being obtained between the model predictions and the experimental measurements. The main novelty of this work is that the free surface dynamics are studied using the volume-of-fluid method and the experimentally scanned gravel bed topography is used in the model. The Cartesian cut-cell method on a structured grid has been used to represent the actual complex 3D bed topography in the numerical model, with the topography obtained using the detailed digital elevation method, which differs from previous studies for well-defined roughness and other boundary-fitted grids. In addition, the deformable free surface has been captured using the VOF method, which is different from the rigid lid approximation being used in most open-channel flow simulations.

The principal flow features measured in the experiments are reasonably reproduced for three different submergence cases, including: the distributions of mean streamwise velocities, turbulence intensities, and Reynolds stresses. The instantaneous flow field, free surface evolution and vortical structures are presented for the low submergence case, in which the roughness has the most significant effect on the flow field. It is shown that the LES is able not only to match the quantitative turbulence data, but also to reflect actual velocity structural patterns seen in the laboratory, illustrating the turbulent chaotic flow structures within open-channel flows and also the effect of a rough bed on the flow depth. It has been found that there are some slight discrepancies in the turbulence statistics, which might be attributed to the periodic boundary conditions used in the simulations and different spatial averaging.

The study demonstrates the capability of the present LES model to provide reliable detailed flow characteristics along with the water depth, which is necessary in order to obtain a better understanding of the turbulent flow dynamics in rough open-channel flows.

Acknowledgements

We would like to thank the EPSRC projects (EP/G014264/1, EP/R022135/1 and EP/S016376/1) and the Royal Society Newton Advanced Fellowship (NAF/R1/201156) for helping to fund this work. Discussion with Professor T. Stoesser and comments of Associate Editor and three anonymous reviewers are gratefully appreciated.

Notation

α	= angle of the channel bed to the horizontal
C_d	= dynamic subgrid coefficient
C	= roughness parameter
F	= volume fraction
Fr	= Froude number
f	= friction factor
g	= gravity acceleration
h	= water depth
H	= maximum gravel bed height
L_x	= computational domain length
L_y	= computational domain height
L_z	= computational domain width
L_{ij}	= tensor used in dynamic subgrid model
M_{ij}	= tensor used in dynamic subgrid model
\bar{p}	= filtered pressure
Re	= Reynolds number
\bar{S}_{ij}	= filtered strain-rate tensor
S	= channel slope
t	= time
U_{bulk}	= mean bulk flow velocity
\bar{u}_i	= resolved velocity components
$\sqrt{u'^2}$	= turbulence intensity
$-u'v'$	= Reynolds stress
u^+	= velocity in wall units
u^*	= friction velocity
$\sqrt{v'^2}$	= turbulence intensity
x_i	= Cartesian coordinates
x	= streamwise direction
y	= vertical direction
z	= spanwise direction
Δx	= mesh size in the streamwise direction
Δy	= mesh size in the vertical direction
Δz	= mesh size in the spanwise direction
θ	= function in the cut-cell method
ρ	= density of the fluid
ρ^w	= density of water
ρ^a	= density of air
μ	= dynamic viscosity of the fluid
μ^w	= dynamic viscosity of water
μ^a	= dynamic viscosity of air
μ_t	= turbulent eddy viscosity
τ_{ij}	= SGS stress tensor
$\bar{\Delta}$	= filter length scale
ϕ	= arbitrary variable
$\bar{\phi}$	= time-averaged variable
ϕ'	= fluctuation with respect to the time-averaged variable
$\langle \phi \rangle$	= spatial averaged variable
$\langle \phi \rangle_x$	= streamwise-averaged variable
$\langle \phi \rangle_y$	= depth-averaged variable
$\langle \phi \rangle_z$	= spanwise-averaged variable

References

- Alfonsi, G., Ferraro, D., Lauria, A., & Gaudio, R. (2019). Large-eddy simulation of turbulent natural-bed flow. *Physics of Fluids*, *31*, 085105.
- Bathurst, J. C. (1985). Flow resistance estimation in mountain rivers. *Journal of Hydraulic Engineering-ASCE*, *111*, 625-643.
- Calhoun, R. J., & Street, R. L. (2001). Turbulent flow over a wavy surface: Neutral case. *Journal of Geophysical Research-Oceans*, *106*(C5), 9277-9293.
- Cameron, S., Nikora, V., & Stewart, M. (2017). Very-large-scale motions in rough-bed open-channel flow. *Journal of Fluid Mechanics*, *814*, 416-429.
- Cooper, J. R., & Tait, S. J. (2008). The spatial organisation of time-averaged streamwise velocity and its correlation with the surface topography of water-worked gravel beds. *Acta Geophysica*, *56*(3), 614-641.
- Cui, J., Patel, V. C., & Lin, C. L. (2003). Large-eddy simulation of turbulent flow in a channel with rib roughness. *International Journal of Heat and Fluid Flow*, *24*(3), 372-388.
- Ferguson, R. (2007). Flow resistance equations for gravel- and boulder-bed streams. *Water Resources Research*, *43*, 1-12.
- Ferraro, D., Coscarella, F., & Gaudio, R. (2019). Scales of turbulence in open-channel flows with low relative submergence. *Physics of Fluids*, *31*, 125114.
- Ferraro, D., Servidio, S., & Gaudio, R. (2019). Velocity scales in steady-nonuniform turbulent flows with low relative submergence. *Environmental Fluid Mechanics*, *19*, 1025-1041.
- Forooghi, P., Stroh, A., Magagnato, F., Jakirlic, S., & Frohnappel, B. (2017). Toward a universal roughness correlation. *Journal of Fluids Engineering*, *139*(12), 121201.
- Germano, M., Piomelli, U., Moin, P., & Cabot, W. H. (1991). A dynamic subgrid-scale eddy viscosity model. *Physics of Fluids A*, *3*(7), 1760-1765.
- Grass, A. J., Stuart, R. J., & Mansourtehrani, M. (1991). Vortical structures and coherent motion in turbulent-flow over smooth and rough boundaries. *Philosophical Transactions of the Royal Society of London Series A-Mathematical Physical and Engineering Sciences*, *336*(1640), 35-65.
- Guala, M., Hommema, S., & Adrian, R. (2006). Large-scale and very-large-scale motions in turbulent pipe flow. *Journal of Fluid Mechanics*, *554*, 521-542.
- Hardy, R. J., Best, J. L., Lane, S. N., & Carbonneau, P. E. (2009). Coherent flow structures in a depth-limited flow over a gravel surface: The role of near-bed turbulence and influence of reynolds number. *Journal of Geophysical Research-Earth Surfurface*, *114*.
- Hardy, R. J., Best, J. L., Parsons, D. R., & Marjoribanks, T. I. (2016). On the evolution and form of coherent flow structures over a gravel bed: Insights from whole flow field visualization and measurement. *Journal of Geophysical Research-Earth Surfurface*, *121*(8), 1472-1493.
- Hardy, R. J., Lane, S. N., Ferguson, R. I., & Parsons, D. R. (2007). Emergence of coherent flow structures over a gravel surface: A numerical experiment. *Water Resource Research*, *43*(3), W03422.
- Ingram, D. M., Causon, D. M., & Mingham, C. G. (2003). Developments in cartesian cut cell methods. *Mathematics and Computers in Simulation*, *61*(3-6), 561-572.
- Jeong, J., & Hussain, F. (1995). On the identification of a vortex. *Journal of Fluid Mechanics*, *285*, 69-94.
- Jimenez, J. (2004). Turbulent flows over rough walls. *Annual Review of Fluid Mechanics*, *36*, 173-196.
- Jimenez, J. (2018). Coherent structures in wall-bounded turbulence. *Journal of Fluid Mechanics*, *842*, P1.
- Kim, K., & Adrian, R. (1999). Very large-scale motion in the outer layer. *Physics of Fluids*, *11*, 417-422.
- Kostaschuk, R. A., & Church, M. A. (1993). Macroturbulence generated by dunes - fraser-river,

- canada. *Sedimentary Geology*, 85(1-4), 25-37.
- Lamarre, H., & Roy, A. G. (2005). Reach scale variability of turbulent flow characteristics in a gravel-bed river. *Geomorphology*, 68(1-2), 95-113.
- Lawless, M., & Robert, A. (2001a). Scales of boundary resistance in coarse-grained channels: turbulent velocity profiles and implications. *Geomorphology*, 39(3-4), 221-238.
- Lawless, M., & Robert, A. (2001b). Three-dimensional flow structure around small-scale bedforms in a simulated gravel-bed environment. *Earth Surface Processes and Landforms*, 26(5), 507-522.
- Legleiter, C. J., Phelps, T. L., & Wohl, E. E. (2007). Geostatistical analysis of the effects of stage and roughness on reach-scale spatial patterns of velocity and turbulence intensity. *Geomorphology*, 83(3-4), 322-345.
- Li, J., & Li, S. S. (2020). Near-bed velocity and shear stress of open-channel flow over surface roughness. *Environmental Fluid Mechanics*, 20, 293-320.
- Lilly, D. K. (1992). A proposed modification of the germano-subgrid-scale closure method. *Physics of Fluids A*, 4(3), 633-635.
- Liu, Z., Adrian, R. J., & Hanratty, T. J. (2001). Large-scale modes of turbulent channel flow: transport and structure. *Journal of Fluid Mechanics*, 448, 53-80.
- McLean, S. R., & Nikora, V. I. (2006). Characteristics of turbulent unidirectional flow over rough beds: Double-averaging perspective with particular focus on sand dunes and gravel beds. *Water Resources Research*, 42(10).
- McSherry, R., Chua, K., Stoesser, T., & Falconer, R. A. (2016). Large eddy simulations of rough bed open channel flow with low submergence and free surface tracking. In *River flow 2016* (p. 85-90). Taylor and Francis.
- Mittal, R., & Iaccarino, G. (2005). Immersed boundary methods. *Annual Review of Fluid Mechanics*, 37, 239-261.
- Muller, A., & Gyr, A. (1986). On the vortex formation in the mixing layer behind dunes. *Journal of Hydraulic Research*, 24(5), 359-375.
- Nakagawa, H., & Nezu, I. (1981). Structure of space-time correlations of bursting phenomena in an open-channel flow. *Journal of Fluid Mechanics*, 104(Mar), 1-43.
- Nezu, I. (1977). *Turbulent structure in open-channel flows* (Unpublished doctoral dissertation). Kyoto University.
- Nezu, I., & Nakagawa, H. (1993). *Turbulence in open-channel flows*. A.A. Balkema, Rotterdam: IAHR monograph series.
- Nichols, A. (2013). *Free surface dynamics in shallow turbulent flows* (Unpublished doctoral dissertation). University of Bradford.
- Nichols, A., Tait, S. J., Horoshenkov, K. V., & Shepherd, S. J. (2016). A model of the free surface dynamics of shallow turbulent flows. *Journal of Hydraulic Research*, 54(4), 516-526.
- Nikora, V., Goring, D., McEwan, I., & Griffiths, G. (2001). Spatially averaged open-channel flow over rough bed. *Journal of Hydraulic Engineering-ASCE*, 127, 123-133.
- Nikora, V., McEwan, I., McLean, S., Coleman, S., Pokrajac, D., & Walters, R. (2007). Double-averaging concept for rough-bed open-channel and overland flows: Theoretical background. *Journal of Hydraulic Engineering -ASCE*, 133(8), 873-883.
- Nikora, V., Stoesser, T., Cameron, S. M., Stewart, M., Papadopoulos, K., Ouro, P., ... A., F. R. (2019). Friction factor decomposition for rough-wall flows: Theoretical background and application to open-channel flows. *Journal of Fluid Mechanics*, 872, 626-664.
- Papadopoulos, K., Nikora, V., Cameron, S., Stewart, M., & Gibbins, C. (2020). Spatially-averaged flows over mobile rough beds: equations for the second-order velocity moments. *Journal of Hydraulic Research*, 58(1), 133-151.
- Patankar, S. V. (1980). *Numerical heat transfer and fluid flow*. London: Taylor & Francis,.
- Powell, D. M. (2014). Flow resistance in gravel-bed rivers: Progress in research. *Earth-Science Reviews*, 136, 301 - 338.

- Robinson, S. K. (1991). Coherent motions in the turbulent boundary layer. *Annual Review of Fluid Mechanics*, 23, 601-639.
- Rodi, W., Constantinescu, G., & Stoesser, T. (2013). *Large-eddy simulation in hydraulics*. Boca Raton, Florida, U. S.: CRC Press.
- Roussinova, V., Biswas, N., & Balachandar, R. (2008). Revisiting turbulence in smooth uniform open channel flow. *Journal of Hydraulic Research*, 46, 36-48.
- Roy, A. G., Biron, P. M., Buffin-Belanger, T., & Levasseur, M. (1999). Combined visual and quantitative techniques in the study of natural turbulent flows. *Water Resources Research*, 35(3), 871-877.
- Roy, A. G., Buffin-Belanger, T., Lamarre, H., & Kirkbride, A. D. (2004). Size, shape and dynamics of large-scale turbulent flow structures in a gravel-bed river. *Journal of Fluid Mechanics*, 500, 1-27.
- Saccone, D., Napoli, E., Milici, B., & De Marchis, M. (2019). Large eddy simulations of rough turbulent channel flows bounded by irregular roughness: The role of geometrical parameters. In *Ercoftac workshop direct and large eddy simulation* (p. 25-32). Springer.
- Schmeeckle, M. W. (2014). Numerical simulation of turbulence and sediment transport of medium sand. *Journal of Geophysical Research: Earth Surface*, 119, 1240-1262.
- Shah, M. K., Agelinchaab, M., & Tachie, M. F. (2008). Influence of piv interrogation area on turbulent statistics up to 4th order moments in smooth and rough wall turbulent flows. *Experimental Thermal and Fluid Science*, 32(3), 725-747.
- Shvidchenko, A. B., & Pender, G. (2001). Macroturbulent structure of open-channel flow over gravel beds. *Water Resources Research*, 37(3), 709-719.
- Singh, K. M., Sandham, N. D., & Williams, J. J. R. (2007). Numerical simulation of flow over a rough bed. *Journal of Hydraulic Engineering-ASCE*, 133(4), 386-398.
- Smagorinsky, J. (1963). General circulation experiments with the primitive equations: I. the basic experiment. *Monthly Weather Review*, 91(3), 99-164.
- Stoesser, T. (2010). Physically realistic roughness closure scheme to simulate turbulent channel flow over rough beds within the framework of les. *Journal of Hydraulic Engineering-ASCE*, 136(10), 812-819.
- Stoesser, T. (2014). Large-eddy simulation in hydraulics: Quo vadis? *Journal of Hydraulic Research*, 52, 441-452.
- Stoesser, T., Braun, C., Garcia-Villalba, M., & Rodi, W. (2008). Turbulence structures in flow over two-dimensional dunes. *Journal of Hydraulic Engineering-ASCE*, 134(1), 42-55.
- Tamburrino, A., & Gulliver, J. S. (2007). Free-surface visualization of streamwise vortices in a channel flow. *Water Resources Research*, 43(11), W11410.
- Thakkar, M., Busse, A., & Sandham, N. (2017). Surface correlations of hydrodynamic drag for transitionally rough engineering surfaces. *Journal of Turbulence*, 18, 138-169.
- Ubbink, O. (1997). *Numerical prediction of two fluid systems with sharp interfaces* (Unpublished doctoral dissertation). Imperial College of Science, Technology and Medicine.
- Xie, Z. (2012). Numerical study of breaking waves by a two-phase flow model. *International Journal for Numerical Methods in Fluids*, 70(2), 246-268.
- Xie, Z. (2013). Two-phase flow modelling of spilling and plunging breaking waves. *Applied Mathematical Modelling*, 37(6), 3698-3713.
- Xie, Z. (2015). A two-phase flow model for three-dimensional breaking waves over complex topography. *Proceedings of the Royal Society A: Mathematical, Physical & Engineering Sciences*, 471, 20150101.
- Xie, Z., Lin, B., & Falconer, R. (2013). Large-eddy simulation of the turbulent structure in compound open-channel flows. *Advances in Water Resources*, 53, 66-75.
- Xie, Z., Lin, B., & Falconer, R. (2014). Turbulence characteristics in free-surface flow over two-dimensional dunes. *Journal of Hydro-environmental Research*, 8(3), 200-209.
- Xie, Z., Lin, B., Falconer, R., & Maddux, T. (2013). Large-eddy simulation of turbulent open-

- channel flow over three-dimensional dunes. *Journal of Hydraulic Research*, 51(5), 494-505.
- Xie, Z., & Stoesser, T. (2020a). A three-dimensional Cartesian cut-cell/volume-of-fluid method for two-phase flows with moving bodies. *Journal of Computational Physics*, 416, 109536.
- Xie, Z., & Stoesser, T. (2020b). Two-phase flow simulation of breaking solitary waves over surface-piercing and submerged conical structures. *Ocean Engineering*, 213, 107679.
- Xie, Z., Stoesser, T., Yan, S., Ma, Q., & Lin, P. (2020). A Cartesian cut-cell based multiphase flow model for large-eddy simulation of three-dimensional wave-structure interaction. *Computers & Fluids*, 213, 104747.
- Yalin, M. S. (1992). *River mechanics*. Tarrytown, N. Y: Pergamon.
- Yuan, J., & Piomelli, U. (2014). Estimation and prediction of the roughness function on realistic surfaces. *Journal of Turbulence*, 15, 350-365.
- Yue, W. S., Lin, C. L., & Patel, V. C. (2005a). Coherent structures in open-channel flows over a fixed dune. *Journal of Fluids Engineering-Transactions of the ASME*, 127(5), 858-864.
- Yue, W. S., Lin, C. L., & Patel, V. C. (2005b). Large eddy simulation of turbulent open-channel flow with free surface simulated by level set method. *Physics of Fluids*, 17(2):025108.
- Yue, W. S., Lin, C. L., & Patel, V. C. (2006). Large-eddy simulation of turbulent flow over a fixed two-dimensional dune. *Journal of Hydraulic Engineering-ASCE*, 132(7), 643-651.
- Zedler, E. A., & Street, R. L. (2001). Large-eddy simulation of sediment transport: Currents over ripples. *Journal of Hydraulic Engineering-ASCE*, 127(6), 444-452.